Metal diffusion properties of ultra-thin high-k Sc_2O_3 films

M. Pachecka[1,a], C. J. Lee[1,2], J. M. Sturm[1], F. Bijkerk[1]

[1]Industrial Focus Group XUV Optics, MESA+ Institute for Nanotechnology, University of Twente, Drienerlolaan 5, *7522NB* Enschede, the Netherlands

[2]Quantum Transport of Matter Group, MESA+ Institute for Nanotechnology, University of Twente, Drienerlolaan 5, *7522NB* Enschede, the Netherlands

ABSTRACT

The diffusion barrier properties of Sc_2O_3 against metal diffusion were studied. Tin and ruthenium were used as probe materials to study the barrier properties of Sc_2O_3 in thickness ranges that are of relevance for gate materials. Tin deposition and hydrogen radical etching from Sc_2O_3 layers of 0.5-1.5 nm thickness, deposited on Ru, show that these Sc_2O_3 layers effectively block the diffusion of Sn into Ru. We show that Sn adhesion and etching depends strongly on the thickness of the Sc_2O_3 film. The etch-rate is found to be inversely proportional to the Sc_2O_3 layer thickness, which we attribute to Sc_2O_3 becoming a more effective charge transfer barrier at larger thicknesses.

1. INTRODUCTION

Group III based dielectrics, such as scandium oxide (Sc_2O_3)[1] and rare earth scandates [2] e.g. $LaScO_3$ have been studied as

[a] m.pachecka@utwente.nl

possible candidates for high-k dielectric applications, due to their possession of a suitably large optical band gap (5-6 eV). Moreover, Sc_2O_3 has a high dielectric constant (ε= 13) in comparison to SiO_2 (ε = 4.5).[3] Scandium oxide, doped with lanthanum, has been investigated as a high-k gate material for silicon-based integrated circuits.[4] However, much of the interest in Sc_2O_3 has been in applications in AlGaN/GaN devices. Devices, based on AlGaN/GaN without passivation, show significant gate lag effects due to the presence of surface states in the region between the gate and drain contact. Moreover due to large polarization induced field and large conduction band offset, high current density can be achieved with AlGaN/GaN heterostructures. Scandium oxide has attractive band gap and thermal lattice properties for use on GaN.[5] A Sc_2O_3 layer was shown to effectively mitigate the collapse in drain current through passivation of the surface traps.[5, 6] Additionally, it was demonstrated that Sc_2O_3 can be used simultaneously as a gate oxide and as a surface passivation layer for AlGaN/GaN high electron mobility transistors.[7]

However, the gate oxide material must satisfy several criteria: in addition to the electronic function of a gate dielectric, the gate oxide material must maintain a high dielectric constant, and serve as a diffusion barrier against diffusion of material from the top electrode. Furthermore, the gate dielectric must be as thin as possible, so a high resistance to diffusion is critical.

Thus, in addition to the electronic properties of the gate, it is also of importance to understand the Sc_2O_3 diffusion-barrier behavior. The thermal stability of the high-k dielectric material is also of importance, thus, a dielectric material should show good thermal stability, at least at the processing temperatures of the device, and have a low coefficient of thermal expansion.[4, 8, 9]

In order to carry out diffusion studies, we use tin (Sn), a highly mobile metallic probe atom, to test if Sc_2O_3 layers of various thicknesses act as a diffusion barrier. Although Sn is not relevant for high-k dielectric applications we used it due to the fact that Sn has the advantage of forming a volatile hydride, which allows it to be removed from surfaces with hydrogen reactive species.[10] Tin intermixes and/or binds strongly with highly electronegative materials, such as ruthenium (Ru), gold (Au), and silver (Ag). Furthermore, it has been shown that Sn, after it diffuses into the aforementioned materials cannot be etched by atomic hydrogen [11-13], while Sn deposited onto Sc_2O_3 can be completely removed with atomic hydrogen.[14] In this work, we study Sc_2O_3 barriers deposited on top of highly electronegative Ru surfaces, with in situ ellipsometry. The deposition and etching results are understood in the context of a metal-insulator-metal tunnel device.

2. EXPERIMENTAL

Ruthenium and scandium were deposited by direct current (DC) magnetron sputtering from targets with 99.95 % and 99.5 % purity, respectively. First, 4 nm of Ru was deposited onto a silicon wafer. On top of Ru, thin layers of scandium (Sc) with thicknesses of 0.5, 1, and 1.5 nm were deposited (see Table 1). An additional sample with 4 nm of Ru, deposited on a silicon wafer, was used as a reference for analysis with low-energy ion scattering spectroscopy (LEIS) measurements (see below). Deposition was performed in a vacuum chamber with a base pressure of $3 \cdot 10^{-8}$ mbar and a temperature of 22 ˚C inside the chamber. Samples were placed approximately 30 cm from the magnetron. The magnetron current during deposition was 1 A while magnetron voltage was 460 V and 410 V for Ru and Sc deposition, respectively. Argon pressure during sputtering was measured to be $7 \cdot 10^{-4}$ mbar during Ru deposition and $6 \cdot 10^{-4}$ mbar during Sc deposition. The deposition rates for Ru and Sc were 0.169 and 0.166 nm/s, respectively.

Table 1. Material and thicknesses composition of the samples. All materials were deposited on silicon wafer substrates.

Material (nm)	**Sample name**		
	0.5Sc_2O_3/Ru	**1Sc_2O_3/Ru**	**1.5Sc_2O_3/Ru**
Sc	0.5	1	1.5
Ru	4	4	4

For many materials, oxidation of the layer is usually self-limiting at atmospheric pressure and room temperature, resulting in a so-called native oxide layer with a thickness of

few nanometers at most. It was reported that 5.5 nm Sc, deposited on a silicon wafer, has a native oxide thickness of 3.6 nm, while 3 nm of Sc is fully oxidized.[11, 14] Thus, Sc layers with a thickness below 3 nm can be expected to fully oxidize when exposed to ambient. However, to test thinner layers, the oxide layer should be terminated. Hence the Sc was deposited on Ru, a noble metal. Ruthenium does not oxidize easily, thus allowing a sharp interface between Ru and Sc native oxide to be created. After deposition, all the samples were removed from the chamber and exposed to ambient conditions to form Sc_2O_3 layers. The properties of the deposited layers were then analyzed with LEIS, and x-ray photoelectron spectroscopy (XPS). Tin deposition and etching experiments were performed in an apparatus that has been described in detail elsewhere.[11] Tin (Umicore) with a bulk density of 7.3 g/cm^3 and purity of 99.9 % was evaporated from an Effusion Cell EF 40C1 (PREVAC) evaporator operated at 980˚C. The Sn deposition rate was calibrated using a quartz microbalance (INFICON XTM/2 Deposition Monitor). It was found that the evaporation rate as measured using the quartz microbalance (QMB) at 980˚C was approximately 0.4 nm/min. Approximately 8 nm of tin was evaporated onto the sample and, immediately afterwards, etched with hydrogen radicals ($H^\cdot$). The $H^\cdot$ flux is generated by passing a molecular hydrogen flow (100 sccm) over a tungsten (W) filament that is heated to 2000˚C. The hydrogen radical flux was calculated to be 10^{17} at /s·cm^2 at the

sample surface from the measured carbon etching rate, following the method used in ref. 15. The temperature of the sample was monitored using a Pt-100 temperature sensor, mounted on the backside of the sample. During hydrogen etching, the filament was operated in 5 min cycles to avoid excessive sample heating. As a result, the temperature modulations were less than 25 ˚C, and the maximum sensor temperature was always below 55 ˚C. Thus, the surface temperature is unlikely to be more than (55+5) ˚C than the sensor temperature. During Sn deposition and etching, the sample was monitored with in situ ellipsometry. After the Sn deposition and etching experiments, the samples were analyzed ex situ with XPS.

3. RESULTS AND DISCUSSION

3.1. AS DEPOSITED SAMPLE ANALYSIS- LEIS

To ensure that the Sc_2O_3 layer forms a closed film, several samples were analyzed with LEIS. To remove surface contaminants, the samples were sputtered with a dose of $4 \cdot 10^{15}$ 3 keV He^+ ions/cm^2 before analysis. The LEIS spectra after sputtering are presented in Figure 1.

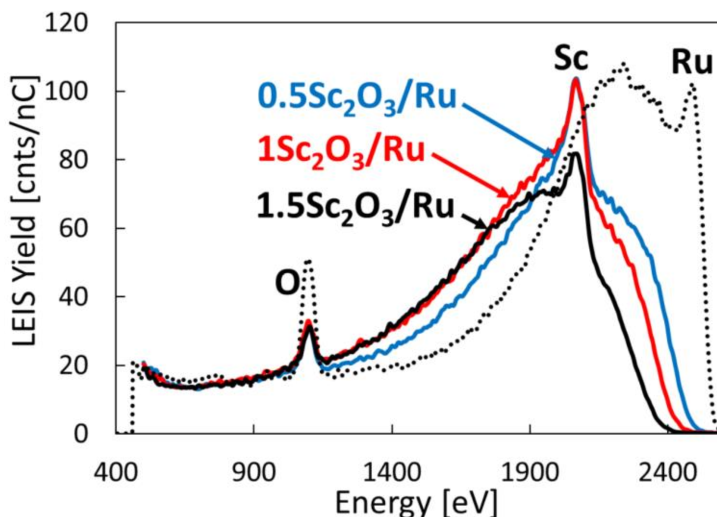

Figure 1. LEIS measurements after mild He sputtering for 0.5Sc_2O_3/Ru (blue solid line), 1Sc_2O_3/Ru (red solid line) and 1.5Sc_2O_3/Ru (black solid line). The dashed line is 4 nm Ru on a silicon wafer, shown as a reference (after the same cleaning step).

It can be seen that, even after mild sputtering of the surface contaminants, the only species present on the surface are Sc and O. No surface Ru was detected for any of the Sc layer thicknesses. This confirms that the prepared Sc native oxide thin layers are uniform and closed layers, thus allowing the oxide layers barrier properties to be studied.

For the different Sc_2O_3 thicknesses, there is a significant difference in the so-called tail signal from sub-surface Ru (especially in the energy range around 2100-2400 eV) . This tail signal results from He ions that penetrate the sample (upon which they are neutralized), backscatter on sub-surface Ru atoms in the direction of the detector and are reionized when

leaving the sample, such that they can be detected with the electrostatic analyzer. Due to stopping of ions in the sample, scattering on a Ru atom deeper inside the sample contributes to the tail signal at lower energy relative to the surface peak. The tail signal thus provides a depth profile of Ru in the sample.[16] For comparison a typical LEIS spectrum for Ru is also presented in Figure 1 as a black dashed line. For 0.5 nm Sc, the thinnest oxide studied, the high energy on-set of the tail signal from sub-surface Ru corresponds to the energy of the Ru surface peak (labelled as Ru) of the Ru reference, which indicates that the Sc_2O_3 layer formed is only just closed, and that Ru is present from the 2nd atomic layer. For thicker Sc_2O_3 layers, the tail and its onset shift to lower energies, which indicates that Ru is covered by a Sc_2O_3 layer free of Ru. Hence, we can conclude that the interface between the Ru and Sc_2O_3 is rather sharp.

From the LEIS measurements, the final thickness values of the Sc_2O_3 layers were obtained, following the procedure described in ref. [16], using an effective stopping value for 3 keV He^+ ions in Sc_2O_3 of 151 eV/nm film thickness extracted from SRIM software. [17] The thicknesses of the top layer differ slightly from the target layer thicknesses. The measured thicknesses of the Sc_2O_3 layers of 0.5Sc_2O_3/Ru, 1Sc_2O_3/Ru and 1.5Sc_2O_3 sample were calculated to be 0.71 nm, 1.10 nm and 1.56 nm, respectively, corresponding to a minor swelling of the nominal thicknesses deposited, due to oxidation.

3.2. TIN DEPOSITION AND ETCHING – IN SITU ELLIPSOMETRY RESULTS

During Sn deposition and etching experiments there is no exposure to ambient, and the etching experiments were performed less than 1 hour after Sn deposition, thus no Sn oxidation is expected. The ellipsometry Delta value at 513 nm is shown for all the samples in Figure 2. Tin deposition starts at 5 minutes, and finishes at 25 minutes, corresponding to a Sn layer that is ~8 nm thick. Afterwards, Sn is etched, starting from 25 minutes, using hydrogen radicals. Etching is performed with the filament operated in 5 minutes cycles to maintain the sample below 55°C. After etching is complete, Delta returns to its original value (apart from a small offset due to the removal of carbon contamination), indicating that Sn does not diffuse through the Sc_2O_3 layer. Remarkably, this is also true for the thinnest Sc_2O_3 layer. The deposited Sn is fully removed from all tested samples, which was confirmed with the XPS measurements. This can be compared to Sn etching experiments on Ru, where the remaining thickness of Sn was reported to be 4.1 nm. [11]

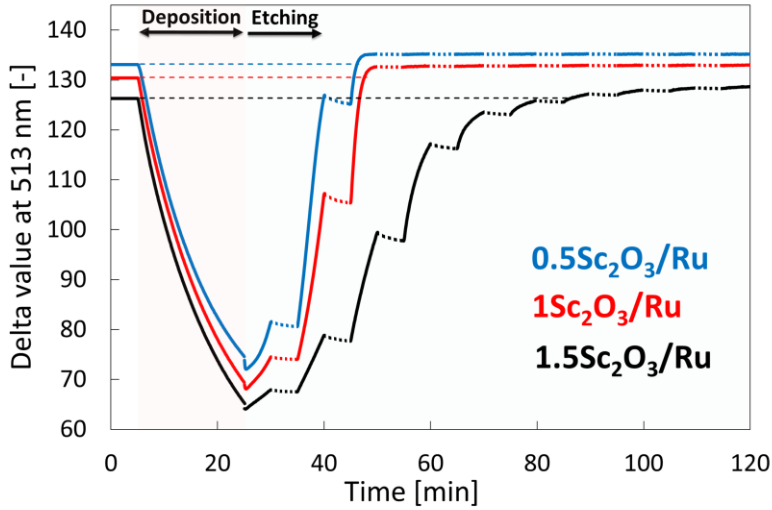

Figure 2. Delta value for 513 nm during Sn deposition and Sn etching. Deposition starts at 5 min and finishes at 25 min. H˙ etching starts at 25 min and proceeds in 5 minutes cycles with the filament ON (solid line) and OFF (dotted line).

It can be seen that the total etching time increases with increasing Sc_2O_3 thickness. The Sn etching time as a function of Sc_2O_3 thickness is presented in Figure 3.

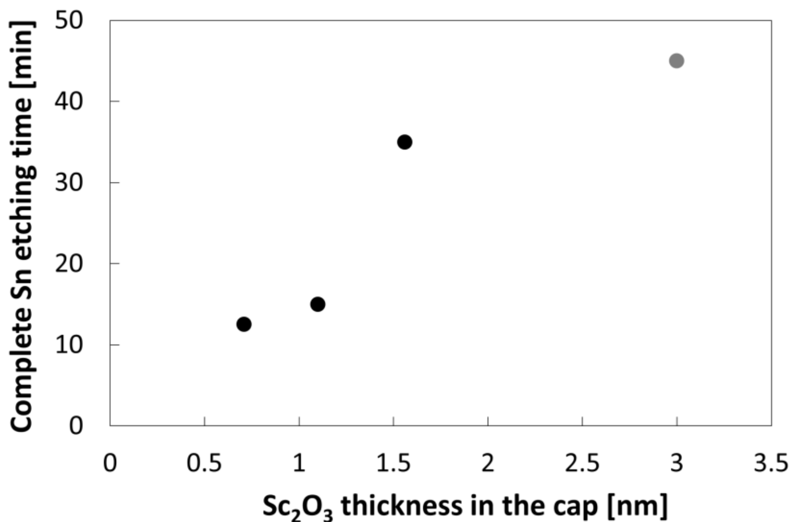

Figure 3. Sn etching time (time when filament was OFF is excluded) as a function of Sc_2O_3 thickness on top of Ru. The point with 3 nm Sc_2O_3 is taken from ref [14]. For this point, the Sc is deposited on a silicon wafer.

The etch-rate is inversely proportional to the Sc_2O_3 layer thickness. Moreover, with increasing Sc_2O_3 thickness, the etching time converges to the value found for bulk Sc_2O_3, which is presented in Figure 3 as the point at 3 nm Sc_2O_3 (obtained from ref. [14]). It should be noted that, for this point, the Sc was deposited on a silicon wafer and full oxidation of the layer was achieved.[14] For etching to be successful, tin hydride must be formed, and charge transfer from the Ru layer to the Sn layer must occur. Hot electrons are generated when atomic hydrogen reacts with Sn, and these may tunnel through the oxide barrier, or get trapped in defect states in the oxide. The tunneling rate depends on the thickness of the Sc_2O_3 layer, and the potential difference between the work functions. Thus, the contribution of tunnelling to the etch rate may be estimated (see below).

3.3. BINDING ENERGY OF Sn TO Sc_2O_3

The binding between Sn and Sc_2O_3 can be understood in terms of charge transfer between the Ru and Sn layers. In this model, the Ru/Sc_2O_3/Sn structure acts as a metal-insulator-metal tunnel device (MIM) and we can compare the Sn etch rate from the tested samples. MIMs consist of a metal back electrode, an insulating oxide layer and metal top layer. The thin insulator

layer acts as high-pass filter for carrier transport.[18-20] Charge transport is limited by the band gap of the insulator, but the small thickness of the oxide layer, and the presence of local defect states in the band gap allow (hot) electrons and holes to tunnel through the oxide barrier.[20] Tunneling from a metal through a thin insulator to another metal has been extensively studied for different material combinations.[18-22] Noting that the Fermi level remains constant across the interfaces, schematic band diagrams for the different thicknesses of Sc_2O_3 can be constructed (see Figure 4 (a), Figure 4 (b) and Figure 4 (c)). The work function values for Ru and Sn were taken to be 4.71 eV and 4.35 eV, respectively [23], while the electron affinity and band gap for Sc_2O_3 are reported to be 0.9 eV[24] and 6.3 eV.[25] The values of the work function, electron affinities and band gap are indicated on a relative scale on the diagrams below.

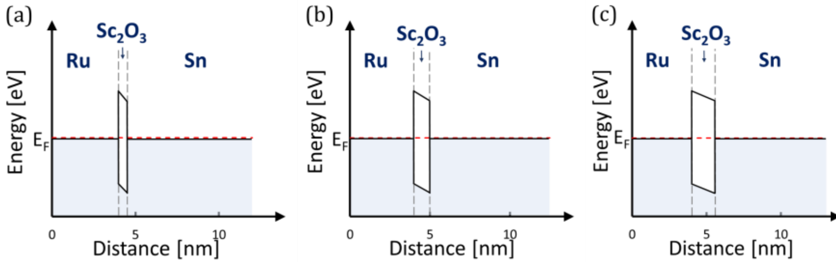

Figure 4. Energy band diagram over the layers for $0.5Sc_2O_3$/Ru (a) $1Sc_2O_3$/Ru (b), and $1.5Sc_2O_3$/Ru (c).

The difference in work functions between Sn and Ru creates a driving potential that favors the diffusion of electrons from Ru to Sn. The potential drop induces an electric field that varies

from 0.51, 0.33 and 0.23 V/nm, depending on the Sc_2O_3 layer thickness.

To estimate the relative tunnelling rates, we consider a plane wave solution to Schrödinger's equation, $\psi_{Ru} = A_1 e^{ik_1 x} + B_1 e^{-ik_1 x}$, for an electron traveling in the x direction in the Ru layer, orthogonal to the Ru/Sc_2O_3 interface. Setting the potential of the Ru layer to zero leads to: $k_1^2 = K_e m_e / \hbar^2$, where K_e is the kinetic energy of the electron, m_e is the electron's mass, and $\hbar$ the reduced Planck's constant. The positive complex exponential represents the wave traveling towards the Sc_2O_3 barrier, while the negative complex exponential represents the reflected wave. In the Sc_2O_3 layer, the wave function is given by $\psi_{ScO} = A_2 e^{ik_2 x} + B_2 e^{-ik_2 x}$, where the electron's momentum is given by $k_2^2 = (K_e - V_a) m_e / \hbar^2$ and V_a is the height of the potential barrier at the Ru/Sc_2O_3 interface. The positive complex exponential represents the transmitted wave function, while the negative complex exponential represents a wave traveling from the Sc_2O_3 into the Ru. In considering electron tunneling from Ru to Sn, we set $B_2 = 0$. To satisfy Schrödinger's equation both the wave function, and it's first derivative must be continuous across the interface. This leads to the following expression for the transmitted and reflected amplitudes, A_2 and B_1, respectively.

$$\mathrm{B_1 = A_1 \frac{ik_1 - k_{2r}}{k_{2r} + ik_1}} \qquad (1)$$

and

$$A_2 = A_1 \frac{i2k_1}{k_{2r}+ik_1} \tag{2}$$

where we have assumed that $V_a > K_e$ and k_{2r} indicates that the momentum should be evaluated at the Ru/Sc_2O_3 interface.

Inside the Sc_2O_3, the electron's momentum becomes complex, leading to an exponentially decaying wave function. As before, the wave function and its derivative should be continuous at the Sc_2O_3/Sn barrier, giving:

$$B_{2s} = A_2 \frac{ik_1 - k_{2s}}{k_{2s}+ik_1} e^{-\overline{k_2}t} \tag{3}$$

$$A_3 = A_2 \frac{i2k_1}{k_{2s}+ik_1} e^{-\overline{k_2}t} \tag{4}$$

where $B_{2s}$is the reflection coefficient from the Sc_2O_3/Sn interface, and k_{2s} is the electron momentum, evaluated at the Sc_2O_3/Sn interface. The bar indicates that the average momentum in the Sc_2O_3 layer should be used. Furthermore, we have also assumed that the potential difference between the Sn layer and the Ru layer is the same as the work function difference between the two materials. From Equations (2) and (4) the amplitude of the electron wave function in the Sn layer can be estimated as:

$$A_3 = -\frac{4k_1^2 e^{-\overline{\overline{k_2}}t}}{(k_{2r}+ik_1)(k_{2s}+ik_1)} \tag{5}$$

while the transmission probability can be estimated as $1/(|A_3^2|)$, which is shown as a function of the layer thickness (Figure 5 (b)) for 1 eV electrons, and as a function of electron energy (Figure 5 (a)) for a barrier thickness of 0.7 nm. Note that for thermal electrons (K_e ~ 0.025 eV), the transmission

probability is orders of magnitude lower than for electrons with an energy of 1 eV. This implies that the electron flux due to tunneling is negligible for thermal electrons.

In deriving equations (1)-(5), we have assumed that B_2 is negligible. We confirm this by combining equations (2) and (3) to calculate the probability density of the B_2term, due to reflection from the Sc_2O_3/Sn interface. For a layer thickness of 0.7 nm, B_2 is two orders of magnitude less than A_2, indicating that tunneling due to reflected electrons is, indeed, negligible.

To estimate if tunneling is significant, the transmission probabilities in Figure 5 (a) and (b) should be compared to the total number of electrons that need to traverse the barrier and the integrated atomic hydrogen flux. The number of Sn atoms (per unit surface area) is 3×10^{16} cm^{-2}, thus, the total charge transfer per unit area is 9×10^{16} cm^{-2} (assuming SnH_3 is the dominant etch product). The atomic hydrogen dose is simply the fluence (flux integrated over the etch time), which varies from 7.5×10^{17} cm^{-2} to 2.1×10^{20} cm^{-2}. Every hydrogen radical may excite a hot electron that tunnels across the barrier. According to ref. 20 these electrons have an energy smaller than 2 eV, thus, we consider the case of electrons with an energy of 1 eV. For the case of 1 eV electrons, the total expected tunneling charge per unit area ranges from 7.8×10^{16} cm^{-2} to 2.7×10^{13} cm^{-2}, which, for the thinnest layer is comparable to the required charge transfer per unit area. Thus, using this data,

tunneling between Sn and Ru predicts an etch time of 860 s compared to the measured 750 s, which is in good agreement. For thermal electrons, the maximum tunneling charge transfer per unit area is only 1.2×10^{14} cm^{-2} for the thinnest barrier, indicating that only hot electrons can contribute significantly to etching via tunneling.

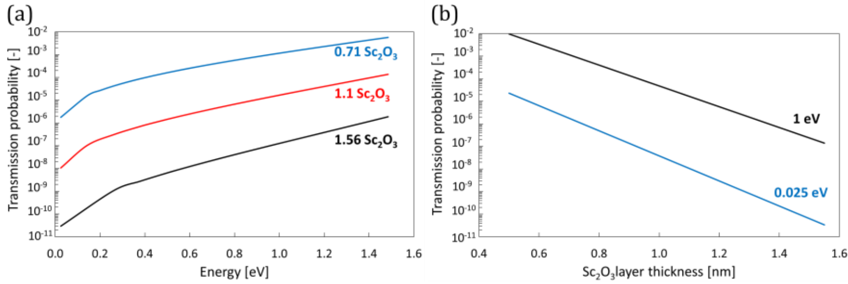

Figure 5. Transmission probability as a function of energy of electrons tunneling from Ru to Sn for different Sc_2O_3 barrier thicknesses (a) and as a function of Sc_2O_3 layer thickness for 1 and 0.025 eV electrons (b).

Reversing the calculation above, we estimate in Figure 6 the contribution of charge transfer between the Sn and Ru layers to Sn etching. The tunneling contribution drops off very rapidly, leaving charge diffusion via defects as the dominant mechanism for most layer thicknesses. This explains the sensitivity for the change of the layer thickness in the etching process. Although the model can take the electron's effective mass into account by replacing m_e with the effective mass, there are, to our knowledge, no reported values of the effective mass of electrons in Sc_2O_3 or Ru. The tunneling probability is most sensitive to the effective mass of the Sc_2O_3 layer. For 1 eV

electrons with effective masses down to 0.5, tunneling is still restricted to the thinnest layer (0.71 nm). However, for 1 eV electrons with effective masses ~0.1, tunneling is efficient for thicknesses up to 1.5 nm.

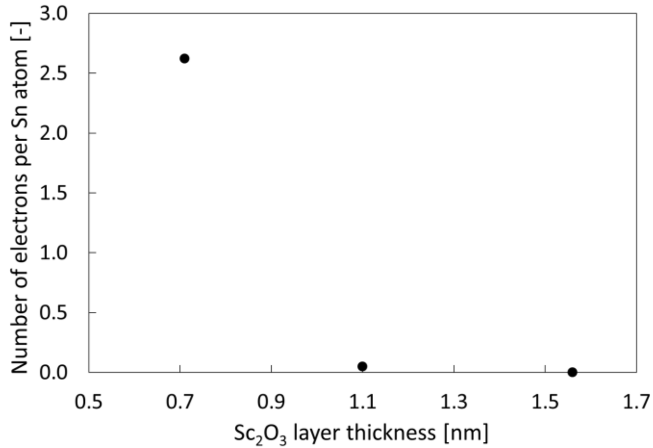

Figure 6. Number of tunneling electrons per Sn atom as a function of Sc_2O_3 layer thickness.

4. CONCLUSIONS

Scandium oxide diffusion barrier properties were tested using a MIM structure, consisting of Ru, Sc_2O_3, and Sn. By depositing, and then etching the Sn layer, it was possible to determine if the Sn diffused through the Sc_2O_3 barrier layer. We observed complete Sn etching from 0.71, 1.1 and 1.56 nm of Sc_2O_3. This demonstrates that even 0.71 nm Sc_2O_3 forms a closed oxide layer that prevents the diffusion of Sn through to the Ru layer.

The Sn etching time was observed to depend on the Sc_2O_3 barrier thickness and increased with increasing Sc_2O_3 thickness. This is explained by the formation of a MIM junction

between the Ru, Sc_2O_3 and Sn, where the built-in potential enhances diffusion of electrons from the Ru and Sc_2O_3 defect states to the Sn. This diffusion of electrons becomes less efficient for larger barrier thicknesses. We use a simple model to show that for thicker layers of Sc_2O_3, the etch rate is limited by charge diffusion, while electron tunneling may contribute significantly for thin layers of Sc_2O_3.

5. ACKNOWLEDGMENT

This work is supported by NanoNextNL, a micro and nanotechnology consortium of the Government of the Netherlands and 130 partners. We acknowledge the support of ASML, Carl Zeiss SMT AG, PANalytical, SolMates, TNO, and Demcon, as well as the Province of Overijssel and the Foundation FOM, now part of NWO (Netherlands Organization of Scientific Research). This work is additionally supported by the CP3E research program of FOM with financial support from NOW. The authors would like to thank Mr. Goran Milinkovic and Mr. John de Kuster, both at ASML, for the technical support, and Mr. Theo van Oijen for sample preparation.

REFERENCES

1. D. O. Klenov, L. F. Edge, D. G. Schlom and S. Stemmer, Applied Physics Letters **86** (5), 051901 (2005).
2. C. Zhao, T. Witters, B. Brijs, H. Bender, O. Richard, M. Caymax, T. Heeg, J. Schubert, V. V. Afanas'ev, A. Stesmans

and D. G. Schlom, Applied Physics Letters **86** (13), 132903 (2005).

3. R. D. Shannon, Journal of Applied Physics **73** (1), 348-366 (1993).
4. P. Sivasubramani, T. H. Lee, M. J. Kim, J. Kim, B. E. Gnade, R. M. Wallace, L. F. Edge, D. G. Schlom, F. A. Stevie, R. Garcia, Z. Zhu and D. P. Griffis, Applied Physics Letters **89** (24), 242907 (2006).
5. B. Luo, J. W. Johnson, J. Kim, R. M. Mehandru, F. Ren, B. P. Gila, A. H. Onstine, C. R. Abernathy, S. J. Pearton, A. G. Baca, R. D. Briggs, R. J. Shul, C. Monier and J. Han, Applied Physics Letters **80** (9), 1661 (2002).
6. B. Luo, J. W. Johnson, B. P. Gila, A. Onstine, C. R. Abernathy, F. Ren, S. J. Pearton, A. G. Baca, A. M. Dabiran, A. M. Wowchack and P. P. Chow, Solid-State Electronics **46** (2002).
7. R. Mehandru, B. Luo, J. Kim, F. Ren, B. P. Gila, A. H. Onstine, C. R. Abernathy, S. J. Pearton, D. Gotthold, R. Birkhahn, B. Peres, R. Fitch, J. Gillespie, T. Jenkins, J. Sewell, D. Via and A. Crespo, Applied Physics Letters **82** (15), 2530 (2003).
8. T. Gupta, *Dielectric Materials in: Copper Interconnect Technology*. (2009).
9. L. Shi, Y. D. Xia, B. Xu, J. Yin and Z. G. Liu, Journal of Applied Physics **101** (3), 034102 (2007).
10. B. M. La Fontaine, J. Sporre, R. E. Lofgren, D. N. Ruzic, O. V. Khodykin, D. W. Myers and P. P. Naulleau, **7969**, 796929-796929-796929 (2011).
11. M. Pachecka, J. M. Sturm, R. W. E. van de Kruijs, C. J. Lee and F. Bijkerk, AIP Advances **6** (7), 075222 (2016).

12. M. M. J. W. van Herpen, D. J. W. Klunder, W. A. Soer, R. Moors and V. Banine, Chemical Physics Letters **484** (4-6), 197-199 (2010).
13. W. A. Soer, M. M. J. W. van Herpen, M. J. J. Jak, P. Gawlitza, S. Braun, N. N. Salashchenko, N. I. Chkhalo and V. Y. Banine, J. Micro/Nanolith. MEMS MOEMS **11** (2), 021118-021111 (2012).
14. M. Pachecka, C. J. Lee, J. M. Sturm and F. Bijkerk, AIP Advances **7** (8), 085107 (2017).
15. O. V. Braginsky, A. S. Kovalev, D. V. Lopaev, E. M. Malykhin, T. V. Rakhimova, A. T. Rakhimov, A. N. Vasilieva, S. M. Zyryanov, K. N. Koshelev, V. M. Krivtsun, M. van Kaampen and D. Glushkov, J. Appl. Phys. **111** (9), 093304 (2012).
16. H. H. Brongersma, *Low-Energy ion scattering in: Characterization of Materials*. (J. wiley & Sons, 2012).
17. J. F. Ziegler, M. D. Ziegler and J. P. Biersack, Nuclear Instruments and Methods in Physics Research Section B: Beam Interactions with Materials and Atoms **268** (11-12), 1818-1823 (2010).
18. J. G. Simmons, J. Phys. D: Appl. Phys. **4**, 613-657 (1971).
19. J. G. Simmons, J. Appl. Phys. **34** (6), 1793-1803 (1963).
20. P. Thissen, B. Schindler, D. Diesing and E. Hasselbrink, New J. Phys. **12** (11), 113014 (2010).
21. L. A. Kasprzak, R. B. Laibowitz and M. Ohring, J. Appl. Phys. **48** (10), 4281-4286 (1977).
22. T. E. Hartman, J. Appl. Phys. **35** (11), 3283-3294 (1964).
23. J. Speight, *Lange's Handbook of Chemistry*, Sixteenth Edition ed. (McGraw-Hill Education, 2005).

24. P. S. P., C. R. Abernathy and F. Ren, *Gallium Nitride Processing for Electronics, Sensors and Spintronics*. (Springer, 2006).
25. A. V. Emeline, G. V. Kataeva, V. K. Ryabchuk and N. Serpone, J. Phys. Chem. B **103**, 9190-9199 (1999).